

## Coupling between the spatially separated magnetism and the topological band revealed by magnetotransport measurements on $\text{EuMn}_{1-x}\text{Zn}_x\text{Sb}_2$ ( $0 \leq x \leq 1$ )

Yuanying Xia,<sup>1,\*</sup> Lin Wang<sup>2,\*</sup> Yuanhao Zhu,<sup>3</sup> Liyu Zhang,<sup>1</sup> Yan Liu,<sup>4</sup> Xueliang Wu,<sup>1</sup> Long Zhang,<sup>1</sup> Tianran Yang,<sup>1</sup> Kunya Yang,<sup>1</sup> Mingquan He,<sup>1</sup> Yisheng Chai,<sup>1</sup> Huixia Fu,<sup>3,†</sup> Xiaoyuan Zhou,<sup>1,‡</sup> and Aifeng Wang<sup>1,§</sup>

<sup>1</sup>Low Temperature Physics Laboratory, College of Physics and Center of Quantum Materials and Devices, Chongqing University, Chongqing 401331, China

<sup>2</sup>Department of Physics, University of Konstanz, D-78457 Konstanz, Germany

<sup>3</sup>College of Physics and Center of Quantum Materials and Devices, Chongqing University, Chongqing 401331, China

<sup>4</sup>Analytical and Testing Center, Chongqing University, Chongqing 401331, China



(Received 23 May 2023; revised 14 September 2023; accepted 25 September 2023; published 11 October 2023)

We study the coupling between topological bands and two distinct magnetic sublattices in  $\text{EuMn}_{1-x}\text{Zn}_x\text{Sb}_2$  ( $0 \leq x \leq 1$ ) using a combination of magnetotransport measurements and density functional theory (DFT) calculations. Hall measurements reveal a low carrier concentration with high mobility across all samples, allowing the observation of quantum oscillation in the range of  $0 \leq x \leq 0.8$  at a relatively low magnetic field. Upon analyzing the quantum oscillation data, the fast Fourier transform spectra for  $0 \leq x \leq 0.8$  exhibit a relatively weak Zn doping dependency but a significant temperature dependency. This weak Zn doping dependency suggests that the magnetotransport properties of  $\text{EuMn}_{1-x}\text{Zn}_x\text{Sb}_2$  are dominated by quasi-two-dimensional small Fermi pockets originating from the Sb zigzag chains, which remain largely unaffected by varying Mn content. The significant temperature-dependent phase of the oscillation indicates that the topological state is tunable by the magnetism of Eu. Our observations suggest that the topological bands arising from Sb zigzag chains are sensitive to adjacent Eu magnetism but are relatively insensitive to more distant Mn atoms. Our experimental results are in good agreement with the DFT calculations, which show that Zn doping introduces only minor electron-type carriers at the Fermi level without substantially altering the Dirac bands. Our study will be helpful for understanding the mechanism of coupling between spatially separated magnetism and topological bands, offering insights that could be valuable for the design of materials with magnetism-tunable topological electronic structures.

DOI: [10.1103/PhysRevB.108.165115](https://doi.org/10.1103/PhysRevB.108.165115)

### I. INTRODUCTION

Magnetic topological materials have recently attracted intense attention in condensed matter physics because they pave a new path to control electronic transport properties by utilizing the interplay between magnetism and topology [1,2]. The layered 112 pnictides, denoted as  $\text{AMn}Pn_2$  ( $A = \text{Ca, Sr, Ba, Eu, or Yb}$ ;  $Pn = \text{Sb or Bi}$ ), serve as a fertile platform for investigating magnetic topological semimetals due to their structural and magnetism diversity [3]. The crystal structure of  $\text{AMn}Pn_2$  is featured by alternating layers of  $A$ ,  $Pn$ , and  $\text{Mn}Pn$ , arranged in the sequence of  $-A/\text{Mn}Pn/A/Pn-$  along the out-of-plane direction.  $Pn$  zigzag chains/square net is the key structural motif that hosts the Dirac band, which has been proven to be a good building block for designing new Dirac semimetals [3,4]. Layers of  $A$  and  $\text{Mn}Pn$  act as buffer layers that affect the physical properties of  $\text{AMn}Pn_2$  through their coupling with the  $Pn$  layer [5]. This coupling between the magnetism in the  $A$  or  $\text{Mn}Pn$  layer and the Dirac band

in the  $Pn$  layer gives rise to various exotic transport phenomena. Examples include the quantum Hall effect observed in  $\text{EuMnBi}_2$  and  $\text{BaMnSb}_2$  [6,7], time-reversal-symmetry breaking Weyl fermion in  $\text{SrMnSb}_2$  and  $\text{YbMnBi}_2$  [8,9], and giant anisotropic magnetoresistance (AMR) in  $\text{EuMnSb}_2$  [10]. However, the systematic investigation of the coupling strength between magnetism in the  $A/\text{Mn}Pn$  layer and the topological band in the  $Pn$  layer is currently lacking.

$\text{EuMnSb}_2$  emerges as an ideal candidate for such investigations. Its structure includes Sb zigzag chains and two spatially separated antiferromagnetic (AFM) sublattices [11–14]. This spatial separation enables independent tuning of the topological bands and two types of magnetic sublattices through chemical doping. Our recent study on  $\text{EuMn}_{1-x}\text{Zn}_x\text{Sb}_2$  ( $0 \leq x \leq 1$ ) focuses on the magnetic properties, establishing magnetic phase diagrams along two principal crystallographic axes [15]. We found that Zn doping at the Mn site can indirectly influence the orientation of Eu moments through the interaction between the Eu and Mn sublattices [15]. However, it still remains unclear how variations in the magnetic structures of Eu and/or Mn affect the topological bands. Fortunately, the low carrier density with high mobility in  $\text{EuMn}_{1-x}\text{Zn}_x\text{Sb}_2$  enables the exploration of the electronic band structure and its relationship with Eu/Mn magnetism via quantum oscillations in our experimental field range [14,16].

\*These authors contributed equally to this work.

†hxfu@cqu.edu.cn

‡xiaoyuan2013@cqu.edu.cn

§afwang@cqu.edu.cn

In this paper, we have carried out a comprehensive magnetotransport and density functional theory (DFT) calculations study on  $\text{EuMn}_{1-x}\text{Zn}_x\text{Sb}_2$  ( $0 \leq x \leq 1$ ). Our Hall measurements reveal that the transport properties of  $\text{EuMn}_{1-x}\text{Zn}_x\text{Sb}_2$  are dominated by the hole-type carriers in the range of  $0 \leq x \leq 0.8$  and reverse to electron-type carriers when  $x = 1$ , where both hole and electron type carriers display low density and high mobility. Quantum oscillations are observed over a broad doping range ( $0 \leq x \leq 0.8$ ), characterized by quasi-two-dimensional (2D) tiny Fermi pockets with small effective masses. The fast Fourier transform (FFT) spectra and effective mass exhibit a weak dependency on Zn doping, suggesting that the topological bands are largely unaffected by variations in Mn content. Conversely, we observe a significant temperature-dependent phase in the oscillations, implying that the topological bands are tunable by the magnetism of Eu ions. The DFT calculations can well capture the experimental results. By comparing the electronic structures with different doping levels, we find that Zn doping introduces only minor electron-type carriers without significantly altering the topological bands derived from Sb zigzag chains. Therefore, our results indicate that the Dirac band, arising from Sb zigzag chains, is more strongly influenced by the magnetism from neighboring Eu ions than by the more distant Mn ions.

## II. METHODS

### A. Experimental details

$\text{EuMn}_{1-x}\text{Zn}_x\text{Sb}_2$  ( $0 \leq x \leq 1$ ) single crystals were grown via the self-flux method using excess Sb as flux. Detailed procedures for the crystal growth, as well as the structural and magnetic property characterizations, can be found in our previous papers [14,15]. Magnetotransport measurements up to 14 T were performed in a TeslatronPT magnet (Oxford Instruments) equipped with a homemade rotator. Longitudinal resistivity  $\rho_{xx}$  was measured by a standard four-probe method. Hall resistivity  $\rho_{xy}$  was measured by a four-terminal technique. To eliminate the effects of contact misalignment, the longitudinal (Hall) resistivity presented in this paper have been symmetrized and antisymmetrized, respectively.

### B. Theoretical methods

To investigate the electronic structure of  $\text{EuMn}_{1-x}\text{Zn}_x\text{Sb}_2$  ( $0 \leq x \leq 1$ ), first-principles calculations were performed with the projected augmented-wave method as implemented in the Vienna *Ab initio* Simulation Package (VASP) [17,18]. In order to introduce the chemical substitutions of the Mn site with Zn, various supercells with doping levels of  $x = 0, 0.25, 0.375, 0.625$ , and 1 were considered, corresponding to the replacement of zero, two, three, five, and eight of eight equivalent Mn sites in a  $1 \times 2 \times 1$  supercell by Zn atoms, respectively. Further details on the supercells can be found in Fig. S1 and Table S1 of the Supplemental Material [19]. In the density functional theory (DFT) calculations, the generalized gradient approximation (GGA) of Perdew-Burke-Ernzerhof (PBE) type was used to treat the exchange-correlation interaction [20]. The cutoff energy for the wave functions was set to 350 eV. The self-consistent convergence threshold for total energy was set at  $10^{-5}$  eV. During structural relaxations, we

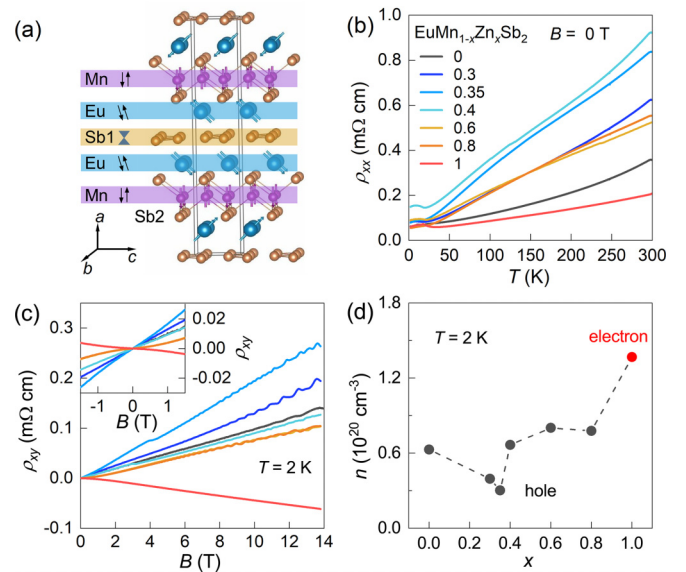


FIG. 1. (a) Crystal and magnetic structures of  $\text{EuMn}_{1-x}\text{Zn}_x\text{Sb}_2$ ; the detailed magnetic structure of the Eu sublattice depends on the temperature, magnetic field, and Zn content  $x$  [15]. Sb1 and Sb2 denote the Sb bonded with Sb and Mn, respectively. The Sb1 layer, where the Dirac band resides, is structurally sandwiched between the antiferromagnetic Eu and Mn layers, which order antiferromagnetically below 19 K and 326 K, respectively. (b) The temperature dependence of resistivity for  $\text{EuMn}_{1-x}\text{Zn}_x\text{Sb}_2$ . (c) Magnetic field dependence of Hall resistivity  $\rho_{xy}(B)$ . (d) The carrier concentration obtained by a linear fit of  $\rho_{xy}(B)$ ; the black and red symbols denote the hole- and electron-type carriers, respectively.

used the experimental lattice parameters listed in Table S1 of the Supplemental Material [19]. All atoms were allowed to relax until the Hellmann-Feynman forces on each atom were below  $0.01$  eV/ $\text{\AA}$ . A  $\Gamma$ -centered grid of  $1 \times 4 \times 8$   $k$  points was used for Brillouin-zone integration. Spin-orbit coupling (SOC) was considered in all calculations. Additionally, Hubbard correction parameters for Eu (5.0 eV) and Mn (3.0 eV) were applied to describe the localized  $f$  and  $d$  orbitals of Eu and Mn, respectively.

## III. RESULTS AND DISCUSSION

### A. Resistivity and Hall measurements

Figure 1(a) shows the crystal and magnetic structures of  $\text{EuMn}_{1-x}\text{Zn}_x\text{Sb}_2$ . The magnetic structure of  $\text{EuMnSb}_2$  is characterized by two magnetic sublattices: Mn forming a C-type AFM below  $T_{\text{Mn}} = 326$  K and Eu forming a canted AFM below  $T_{\text{Eu1}} = 19$  K [12,13,15]. The detailed magnetic structure, including the spin orientation and stacking sequence, depends on the parameters of Zn content  $x$ , temperature, and magnetic field [15]. An increase in Zn content suppresses  $T_{\text{Mn}}$ , while  $T_{\text{Eu1}}$  remains nearly constant. Additionally, the orientation of Eu moments gradually rotates from the  $a$  axis to the  $bc$  plane as  $x$  increases [15]. Note that the Sb1 zigzag layer, which hosts the Dirac bands, is sandwiched by the  $\text{Eu}^{2+}$  layers. This structural arrangement implies a stronger coupling between the Dirac bands and Eu moments compared to Mn moments.

As shown in Fig. 1(b), the resistivity of  $\text{EuMn}_{1-x}\text{Zn}_x\text{Sb}_2$  generally exhibits metallic behavior with anomalies corresponding to Eu magnetic orderings at low temperatures. The room-temperature resistivity shows a domelike doping dependence on doping levels. The high resistivity in doped samples possibly originates from the strong magnetic fluctuation arising from disordered Mn moments. Previous studies indicate that the resistivity behavior is sensitive to the single-crystal growth method, where both semiconducting and metallic single crystals have been shown [10,21,22]. The metallic resistivity observed in  $\text{EuMn}_{1-x}\text{Zn}_x\text{Sb}_2$  ( $0 \leq x \leq 1$ ) suggests similar single-crystal growth conditions across the doping range studied, illustrating the intrinsic nature for doping-dependent physical properties in our experiments.

Hall measurements were performed to identify the carrier type and carrier density [see Fig. 1(c)]. For  $0 \leq x \leq 0.8$ , the Hall resistivity [ $\rho_{xy}(B)$ ] curves at 2 K show a nearly linear behavior with a positive slope, implying hole-dominant transport. In contrast, for  $x = 1$ , a negative slope is observed, suggesting electron-dominant transport. The inset of Fig. 1(c) indicates a multiband effect for  $0.3 \leq x \leq 1$ , evidenced by a subtle slope change near  $B = 0$  T [23]. The carrier concentration, determined from the single-band linear fit to the high-field regions of  $\rho_{xy}(B)$  curves, decreases initially and then increases with further doping [Fig. 1(d)]. The carrier concentration is low and exhibits a weak doping dependency, varying in a range of  $(0.3\text{--}1.4) \times 10^{-20} \text{ cm}^{-3}$ . This behavior is consistent with isovalent doping since no nominal carriers are introduced by the substitution of  $\text{Mn}^{2+}$  with  $\text{Zn}^{2+}$ . In the semiclassical transport model:  $\tan\theta_H = \rho_{xy}/\rho_{xx} = eB\tau/m^* = \omega_c\tau = \mu B$ , where  $\theta_H$  is the Hall angle,  $\tau$  is the scattering time,  $m^*$  is effective mass,  $\omega_c$  is the cyclotron frequency, and  $\mu$  is the mobility. The  $\tan\theta_H$  vs  $B$  curves are displayed in Fig. S2 in the Supplemental Material [19]. The estimated  $\theta_H$  ranges from  $20^\circ$  to  $60^\circ$  at 2 K and 14 T, suggesting high mobility in crystals across the whole doping range. Therefore, the transport property of  $\text{EuMn}_{1-x}\text{Zn}_x\text{Sb}_2$  is dominated by small Fermi pockets with high mobility, allowing the exploration of its electronic band structure via quantum oscillation at relatively low magnetic fields (5–14 T).

### B. Magnetoresistance analysis

In order to get insight into the electronic band structure of  $\text{EuMn}_{1-x}\text{Zn}_x\text{Sb}_2$ , magnetotransport measurements up to 14 T were performed on  $\text{EuMn}_{1-x}\text{Zn}_x\text{Sb}_2$  ( $0 \leq x \leq 1$ ) single crystals. Clear quantum oscillation is visible for  $0 \leq x \leq 0.8$  (see Fig. 2) but is absent for  $x = 1$  (Fig. S3) [19]. Figures 2(a)–2(f) display the magnetic field dependence of magnetoresistance,  $\text{MR}(B) = [\rho(B) - \rho(0)]/\rho(0) \times 100\%$ , measured at various temperatures with  $B \parallel a$  for  $\text{EuMn}_{1-x}\text{Zn}_x\text{Sb}_2$  ( $x = 0, 0.3, 0.35, 0.4, 0.6, \text{ and } 0.8$ ). Shubnikov–de Haas (SdH) oscillation signals are visible on the  $\text{MR}(B)$  curves when  $B > 6$  T. As seen in Figs. 2(a)–2(f) and Fig. S3(a) [19], the behavior of  $\text{MR}(B)$  curves of  $\text{EuMn}_{1-x}\text{Zn}_x\text{Sb}_2$  ( $0 \leq x \leq 1$ ) exhibits a remarkable doping and temperature dependencies, with typical MR values on the order of 100% at 2 K and 14 T. Note that a slope change or sudden decrease occurs in the low-field region of  $\text{MR}(B)$  curves (2–4 T), coinciding with the spin-flop transition in the magnetization  $M(B)$

data (Fig. S4 in [19]), which is indicative of its magnetic origin.

To deepen our understanding of  $\text{MR}(B)$  curves and underlying electronic structure [24], we quantitatively analyze the  $\text{MR}(B)$  curves using a simple power law  $\text{MR}(B) = AB^m$  [25], where  $A$  is a constant and  $m$  is the power-law exponent. The extracted values of  $m$  are displayed in supplemental Figs. S3(b) and S3(c) [19]. (1) For the doping dependence of  $m$  at 2 K as shown in supplemental Fig. S3(b) [19],  $m$  values are 1.8 and 2.0 for  $x = 0$  and  $x = 0.3$ , respectively. As  $x$  increases to 1,  $m$  first decreases to 0.6 ( $x = 0.8$ ) and then increases back to 1.1 ( $x = 1$ ). (2) For the temperature dependence of  $m$  as shown in supplemental Fig. S3(c) [19],  $m$  values at 2 K range from 0.6 to 2 depending on  $x$ . With increasing temperature,  $m$  decreases/increases to approximately 1 at 75 K and increases linearly to  $\sim 1.5$  with increasing temperature from 75 to 300 K. Briefly, the variations in  $m$  imply that  $\text{MR}(B)$  in  $\text{EuMn}_{1-x}\text{Zn}_x\text{Sb}_2$  with different  $x$  manifests distinct behaviors at low temperatures but converges to linear MR as temperature increases from 2 K to 75 K. It is well known that MR in conventional metal usually exhibits a quadratic magnetic field dependence at low fields and saturates at high fields [24]. Thus the parabolic  $\text{MR}(B)$  curves in  $x = 0$  and 0.3, along with the saturation behavior in  $x = 0.6$  and 0.8, could be understood in the conventional MR scenario. The linear MR can be interpreted in terms of both quantum transport mechanisms, such as Dirac fermion, and classical magnetotransport, such as inhomogeneity or open Fermi surface [26]. Given the quantum oscillation data and calculated electronic structures discussed later, we propose that the linear MR can be taken as a sign for the Dirac semimetal [27].

### C. Temperature dependence of quantum oscillation

Oscillatory components of  $\text{EuMn}_{1-x}\text{Zn}_x\text{Sb}_2$  ( $x = 0, 0.3, 0.35, 0.4, 0.6, \text{ and } 0.8$ ) are extracted by subtracting a third-order polynomial background and plotted against  $1/B$  in Figs. 2(g)–2(l). For  $0.3 \leq x \leq 0.8$ , beat patterns are evident, suggesting the presence of multiple frequencies. As shown in Figs. 2(m)–2(r), The fast Fourier transform (FFT) spectra of these oscillatory components exhibit a similar pattern, showing a main frequency and several higher frequencies with weaker amplitudes.  $F_\alpha = 117$  T in  $\text{EuMnSb}_2$  is consistent with the FFT spectra ( $F = 126$  and 220 T) obtained by quantum oscillation measurements performed with magnetic fields up to 40 T [16]. The absence of  $F = 220$  T frequency in our measurements is due to the fact that the low magnetic field in our measurements cannot induce an observable Zeeman splitting.  $F_\alpha$  at 2 K exhibits a weak domelike doping dependence [Fig. S5(c)] [19], which increases from 117 T in  $x = 0$  to 150 T in  $x = 0.35$  and then decreases to 129 T in  $x = 0.8$ . From the FFT spectra displayed in Figs. 2(m)–2(r), multiple higher frequencies in addition to  $F_\alpha$  are observed for Zn doped samples ( $0.3 \leq x \leq 0.8$ ). From Fig. S5 in [19], one can see that although it is difficult to track the detailed evolution of these frequencies as a function of doping, FFT spectra with a similar general feature can be identified, indicating the electronic structure of  $\text{EuMn}_{1-x}\text{Zn}_x\text{Sb}_2$  is not significantly altered by Zn doping, i.e., insensitive to Mn content. For a typical FFT spectrum at  $x = 0.3$  [Fig. 2(n)],

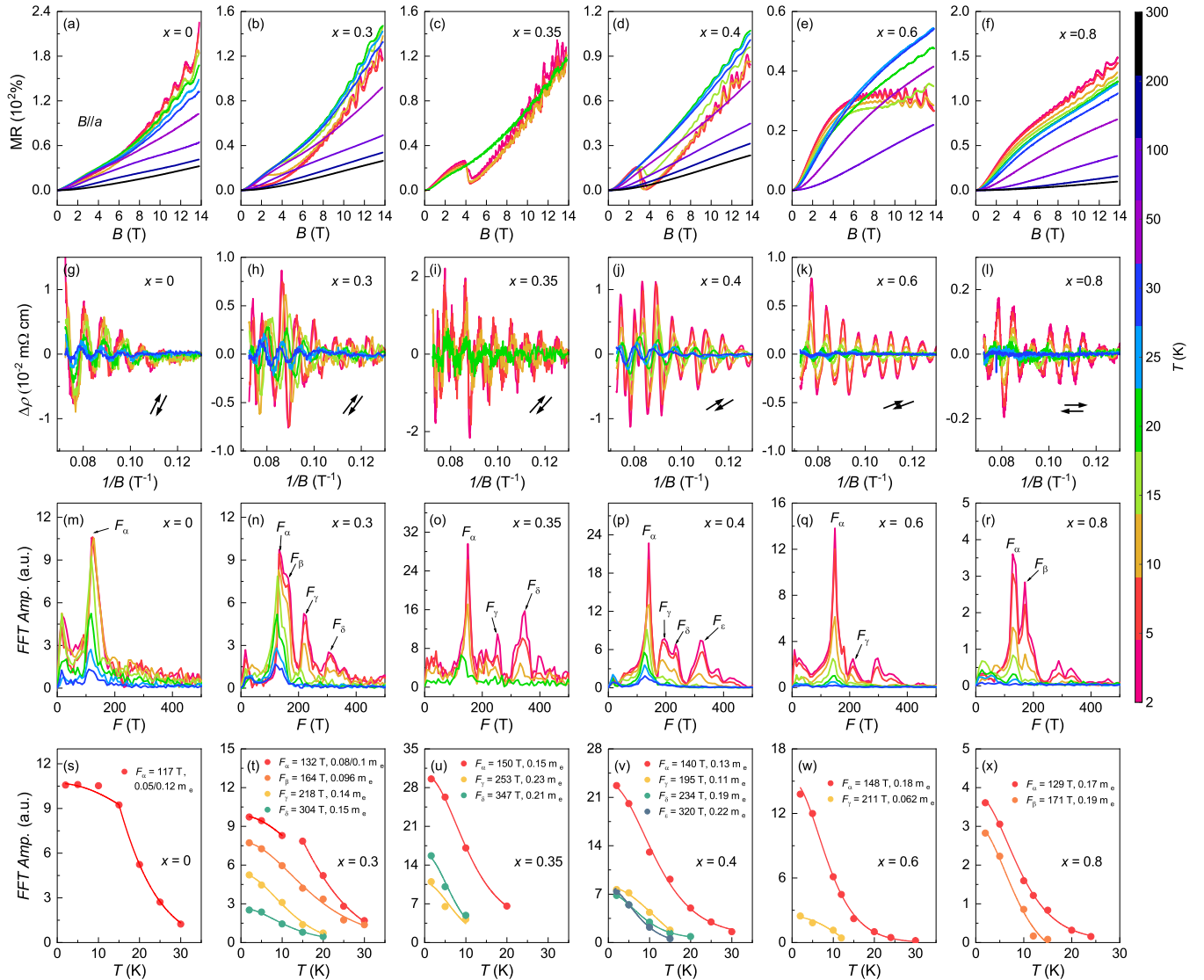


FIG. 2. Temperature dependence of the quantum oscillation in  $\text{EuMn}_{1-x}\text{Zn}_x\text{Sb}_2$  ( $x = 0, 0.3, 0.35, 0.4, 0.6, \text{ and } 0.8$ ). (a)–(f) Magnetic field dependence of MR measured with  $B \parallel a$  at various temperatures (2, 5, 10, 15, 20, 25, and 30 K). (g)–(l)  $\Delta\rho$  as a function of  $1/B$  at various temperatures, which are oscillatory components of resistivity obtained by subtracting polynomial backgrounds from (a)–(f). The arrows in (g)–(l) represent the orientation of Eu moments deduced from the magnetization data; the details can be found in Ref. [15]. (m)–(r) FFT spectra of  $\Delta\rho$  at various temperatures.  $F_\alpha$ ,  $F_\beta$ ,  $F_\gamma$ , and  $F_\delta$  represent harmonic peaks as marked in panels (m)–(r).

four frequencies  $F_\alpha = 132$  T,  $F_\beta = 164$  T,  $F_\gamma = 218$  T, and  $F_\delta = 304$  T are observed. The corresponding extremal cross-sectional area of the Fermi surface  $A_F$  can be estimated by the Onsager relation  $F = (\Phi_0/2\pi^2)A_F$  [28], where  $\Phi_0$  is the flux quantum. The estimated  $A_F$ 's for these frequencies are  $A_{F,\alpha} = 1.26$  nm<sup>2</sup>,  $A_{F,\beta} = 1.57$  nm<sup>2</sup>,  $A_{F,\gamma} = 2.08$  nm<sup>2</sup>, and  $A_{F,\delta} = 2.90$  nm<sup>2</sup>. These Fermi surface areas correspond to 0.61%, 0.76%, 1.01%, and 1.41% of the Brillouin zone in the (100) plane, which is indicative of small Fermi pockets. The results of SdH oscillation measurements are consistent with those of Hall measurements, which indicate Fermi pockets with a relatively weak doping dependence.

The effective mass  $m^* = m/m_e$  can shed light on the band dispersion around the Fermi level ( $E_F$ ) [29], where material with linear dispersion usually has a small effective mass [30]. We extract the effective mass in  $\text{EuMn}_{1-x}\text{Zn}_x\text{Sb}_2$  through the

fit of the temperature dependence of oscillation amplitude to the Lifshitz-Kosevich (LK) thermal damping factor [28]:

$$R_T = \frac{\alpha T m^* / \bar{B}}{\sinh(\alpha T m^* / \bar{B})}, \quad (1)$$

where  $\alpha = 2\pi^2 k_B m_e / e\hbar = 14.69$  T/K and  $1/\bar{B}$  is the average inverse field when performing FFT analysis. As shown in Figs. 2(s)–2(x), all FFT amplitude vs temperature curves can be well fitted by the  $R_T$  damping term, yielding effective masses as detailed in Figs. 2(s)–2(x) and Table I. The effective masses for  $F_\alpha$  and  $F_\beta$  range from 0.12–0.18 $m_e$ , while other frequencies have slightly larger effective masses (0.2–0.3 $m_e$ ). These values of effective masses are comparable to that in (Sr,Yb)MnSb<sub>2</sub> and SrZnSb<sub>2</sub> (0.1 $m_e$ ) [8,23,31], larger than that in (Ca,Ba)MnSb<sub>2</sub> (0.05 $m_e$ ) [32,33], but smaller than that

TABLE I. Parameters derived from the analyses of SdH oscillation data for  $\text{EuMn}_{1-x}\text{Zn}_x\text{Sb}_2$ .

$x$	$T_{\text{Eu1}}$ (K)	$T_{\text{Eu2}}$ (K)	$T_{\text{Mn}}$ (K)	Frequency	$F$ (T)	$m$ ( $m_e$ )	$F_{2\text{D}}$ (T)	$F_{3\text{D}}$ (T)	$F_{3\text{D}}/F_{2\text{D}}$
0	19.08	9.58	326	$F_\alpha$	117	0.05/0.12	119.81	1.32	0.01
0.3	18.30	6.28	245	$F_\alpha$	132	0.08/0.10	103.61	29.45	0.28
				$F_\beta$	164	0.096	98.02	70.42	0.72
				$F_\gamma$	218	0.14	98.69	126.21	1.28
				$F_\delta$	304	0.15			
				$F_\alpha$	150	0.15	133.88	16.81	0.13
0.35	17.58			$F_\gamma$	253	0.23	82.10	177.42	2.16
				$F_\delta$	347	0.21	77.00	275.39	3.58
				$F_\alpha$	140	0.13	98.79	40.25	0.41
0.4	18.07			$F_\gamma$	195	0.11	91.77	99.69	1.09
				$F_\delta$	234	0.19	97.93	143.16	1.46
				$F_\epsilon$	320	0.22	151.56	174.85	1.15
				$F_\alpha$	148	0.18	136.05	13.96	0.10
0.6	19.56			$F_\gamma$	211	0.062			
				$F_\alpha$	129	0.17	139.32	0	0
0.8	19.57			$F_\alpha$	129	0.17	139.32	0	0
				$F_\beta$	171	0.19			

in  $(\text{Ca,Sr,Yb})\text{MnBi}_2$  ( $0.3m_e$ ) [30,34,35]. It is worth noting that the amplitude of  $F_\alpha$  for  $x = 0$  and 0.3 exhibits different thermal damping rates below and above  $T_{\text{Eu1}}$ , indicative of different effective masses. This could be attributed to band dispersion changes caused by Eu AFM ordering [14].

In a nonmagnetic topological semimetal, both the frequency and phase of quantum oscillation are expected to remain constant with varying temperatures. However, in Fig. 2, we observed substantial shifts in the positions of peaks and valleys of quantum oscillations as a function of temperature for  $0 \leq x \leq 0.8$ , i.e., temperature-induced phase shift for the quantum oscillations. The phase shift can be better visualized in Fig. 3, which plots peak/valley positions against temperature. It is well known that the phase of quantum oscillation is related to the Berry phase, which in turn is a key indicator of a topological state. However, the quantitative determination of Berry phase  $\phi_B$  via quantum oscillation phase  $\gamma + \delta$  is a little trick, i.e., different papers use different criteria and the most widely adopted one is that  $\gamma = \frac{1}{2} - \frac{\phi_B}{2\pi}$ , where  $\delta$  is a phase shift determined by the dimensionality of the Fermi surface and has a value of 0 for 2D cases and  $\pm \frac{1}{8}$  for 3D cases [36]. Although the determination of the absolute value for the Berry phase is challenging, the existence of temperature-induced phase shift is evident, suggesting a topological phase transition. However, whether the Berry phase transitions from trivial to nontrivial or vice versa cannot be definitively concluded due to uncertainties in its absolute value. Moreover, through a careful inspection of the FFT spectra [Figs. 2(m)–2(r)], a slight frequency shift as a function of temperature is also detected by the FFT spectra. Such significant temperature dependencies in oscillation phase and frequency have also been observed in magnetic topological semimetals with a low carrier density such as  $\text{MnBi}_{2-x}\text{Sb}_x\text{Te}_4$ ,  $\text{PrAlSi/NdAlSi}$ , and  $\text{CePtBi}$  [37–40]. This phenomenon has been interpreted within the framework of coupling between magnetic order and topological bands. Therefore, our observations suggest that, in  $\text{EuMn}_{1-x}\text{Zn}_x\text{Sb}_2$ , topological properties could be tuned by manipulating the Eu magnetism.

#### D. Angular dependence of quantum oscillation

To probe the fermiology of  $\text{EuMn}_{1-x}\text{Zn}_x\text{Sb}_2$ ,  $\text{MR}(B)$  were measured at various magnetic field orientations at  $T = 2$  K. The results are displayed in Figs. 4(a)–4(f). The geometry of the measurement setup is depicted in the inset of Fig. 4(a), where  $\theta$  is the angle between  $a$  axis and the applied field. As the magnetic field is tilted away from the  $a$  axis, the value of MR decreases and even turns negative for  $x = 0.6$  and 0.8. Notice that the amplitude of the SdH oscillation diminishes with increasing  $\theta$  and vanishes for  $\theta > 60^\circ$ , which is a characteristic of the 2D Fermi surface.

After background subtraction, the oscillatory pattern  $\Delta\rho$  exhibits a systematic evolution with the rotation of the magnetic field [Figs. 4(g)–4(l)]. Such evolution can be better visualized by the FFT spectra, as shown in Figs. 4(m)–4(r). As the magnetic field rotates from the  $a$  axis to the  $bc$  plane, the FFT frequencies shift systematically toward high frequencies, along with a decrease in FFT amplitude. To quantitatively analyze the angular dependence of oscillation frequencies  $F(\theta)$ , the  $F(\theta)$  curves are fitted to the formula  $F(\theta) = F_{3\text{D}} + F_{2\text{D}}/\cos(\theta)$  [Figs. 4(s)–4(x)], where  $F_{3\text{D}}$  and  $F_{2\text{D}}$  represent the 3D and 2D component, respectively [41]. The fitting results are listed in Table I, where the dimensionality of the Fermi surface can be reflected by the ratio of  $F_{3\text{D}}/F_{2\text{D}}$ . From the  $F_{3\text{D}}/F_{2\text{D}}$  ratio, it is evident that  $F_\alpha$  are of good 2D character ( $F_{3\text{D}}/F_{2\text{D}} < 1$ ), while other frequencies are of quasi-2D character with significant 3D components ( $F_{3\text{D}}/F_{2\text{D}} > 1$ ). From Table I, we can see that the  $F_{3\text{D}}/F_{2\text{D}}$  ratio for  $F_\alpha$  shows a domelike doping dependence, increasing from 0.01 at  $x = 0$  to 0.41 at  $x = 0.4$  and then decreasing to 0 at  $x = 0.8$ . This suggests a doping tunable dimensionality of the Fermi surface.

#### E. Electronic structure calculations

To understand the Zn doping effect and quantum oscillation data, DFT calculations were employed to investigate the electronic structure of  $\text{EuMn}_{1-x}\text{Zn}_x\text{Sb}_2$ . From the band calculations on  $\text{EuMnSb}_2$  [10] and  $\text{EuZnSb}_2$  (see Fig. S6

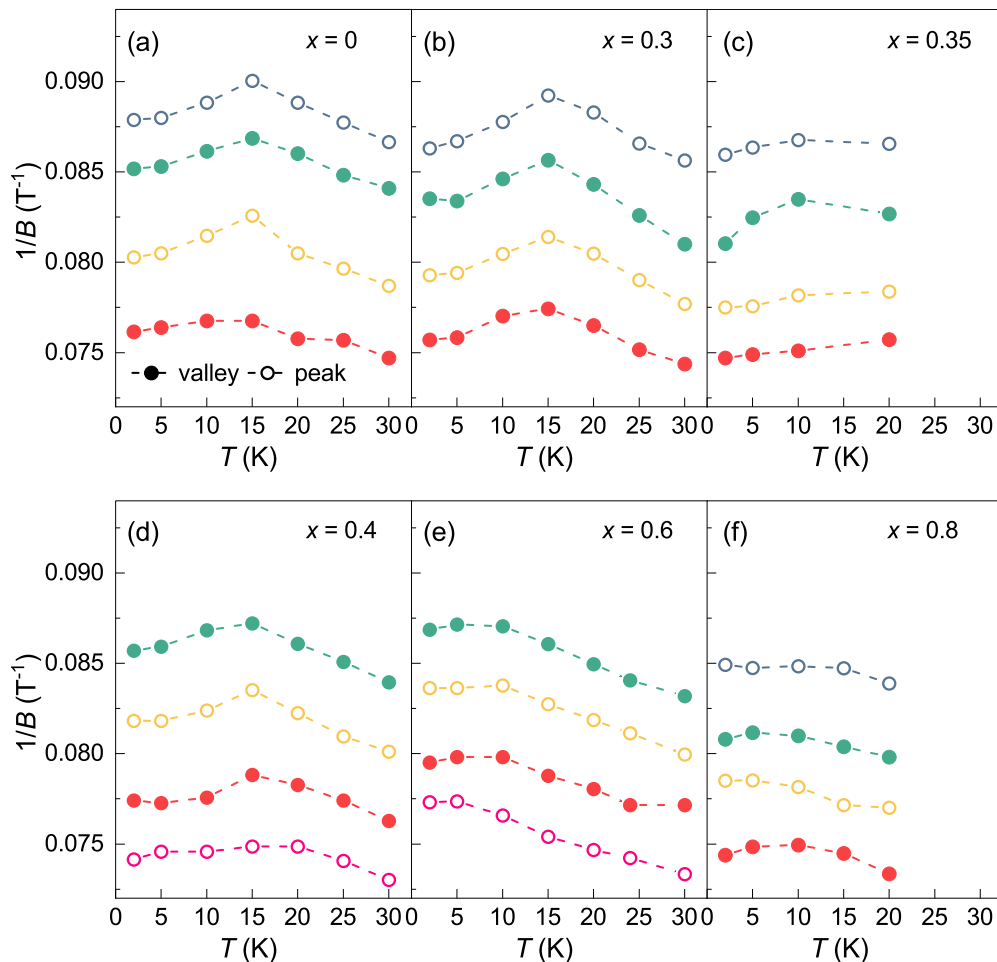


FIG. 3. (a)–(f) Temperature dependence of peak (open symbol) and valley (filled symbol) positions in the oscillatory resistivity  $\Delta\rho$  for  $x = 0, 0.3, 0.35, 0.4, 0.6,$  and  $0.8$ , which are obtained from Figs. 2(g)–2(l).

in [19]), one can see that the orientation of Eu moments has a relatively small influence on the electronic structure of  $\text{EuMnSb}_2/\text{EuZnSb}_2$ . To extract the impact of Zn doping on the electronic structure, a  $1 \times 2 \times 1$  supercell with the same magnetic structure (Fig. S1 in [19]) was adopted for the DFT calculations of  $\text{EuMn}_{1-x}\text{Zn}_x\text{Sb}_2$  ( $x = 0, 0.25, 0.375, 0.625,$  and  $1$ ). The band structures calculated with the pristine chemical cell for the parent compounds  $x = 0$  and  $1$  are also displayed in Fig. S7 in the Supplemental Material [19].

In Fig. 5(a), we show the total density of states (TDOS) curves with different Zn content  $x$ . One can see that Zn doping primarily affects states deep below the Fermi level ( $-10$  to  $-4$  eV). Upon closer inspection of the TDOS around the Fermi level [Fig. 5(b)], a slight Zn doping-induced increase can be recognized. These findings are in good agreement with the Hall measurements, which reveal a low carrier concentration with weak doping dependency [Fig. 1(d)]. The projected density of states (PDOS) analysis [Figs. 5(b) and 5(c)] provides further insights into the Zn doping mechanism. In  $\text{EuMn}_{1-x}\text{Zn}_x\text{Sb}_2$ , Sb exists in two distinct chemical environments: Sb1, which forms zigzag chains with other Sb atoms, and Sb2, which forms an anti-PbO layer with Mn/Zn atoms. Different chemical environments of Sb are manifested as quite different orbital characters: the Dirac bands primarily originate from the Sb1  $p_y$  and  $p_z$  orbitals, while Sb2 states lie

above or below the Fermi level (Fig. S8 in [19]). The Fermi surface of  $\text{EuMn}_{1-x}\text{Zn}_x\text{Sb}_2$  is dominated by the states of Sb1 with a negligibly small contribution from Mn and Sb2. Zn doping mainly increases the states of Zn and Sb2. In Fig. 5(a) and Fig. S9 in the Supplemental Material [19], it is evident that Zn  $3d$  states are localized by forming a narrow impurity band at  $\sim 8$  eV below the Fermi level and only tiny Zn  $4s$  states are presented at the Fermi level. The Zn doping effect in  $\text{EuMn}_{1-x}\text{Zn}_x\text{Sb}_2$  is similar to that in  $\text{BaFe}_{2-x}\text{Zn}_x\text{As}_2$ , where Zn  $3d$  states are localized due to the large energy difference between the  $3d$  states of Zn and Fe [42,43]. The increase of Sb2 orbital contribution to the valence band is possibly induced by the change in hybridization strength between Sb2 and Mn/Zn atoms [44].

Figures 6(b)–6(f) display the orbital resolved band structures for  $\text{EuMn}_{1-x}\text{Zn}_x\text{Sb}_2$  ( $x = 0, 0.25, 0.375, 0.625,$  and  $1$ ). The electronic structures of  $\text{EuMn}_{1-x}\text{Zn}_x\text{Sb}_2$  are consistent with previous reports [10,45] and show typical features of square-net-based Dirac semimetals [3,46]. However, there is a discrepancy between the DFT calculations and magneto-transport measurements; the former suggests an energy gap at the Fermi level for  $x = 0, 0.25,$  and  $0.375$  [Figs. 6(b)–6(d)], inconsistent with observed semimetallic behavior. This discrepancy may stem from crystal defects that shift the Fermi level. The Fermi surface of  $\text{EuMn}_{1-x}\text{Zn}_x\text{Sb}_2$  consists of Fermi

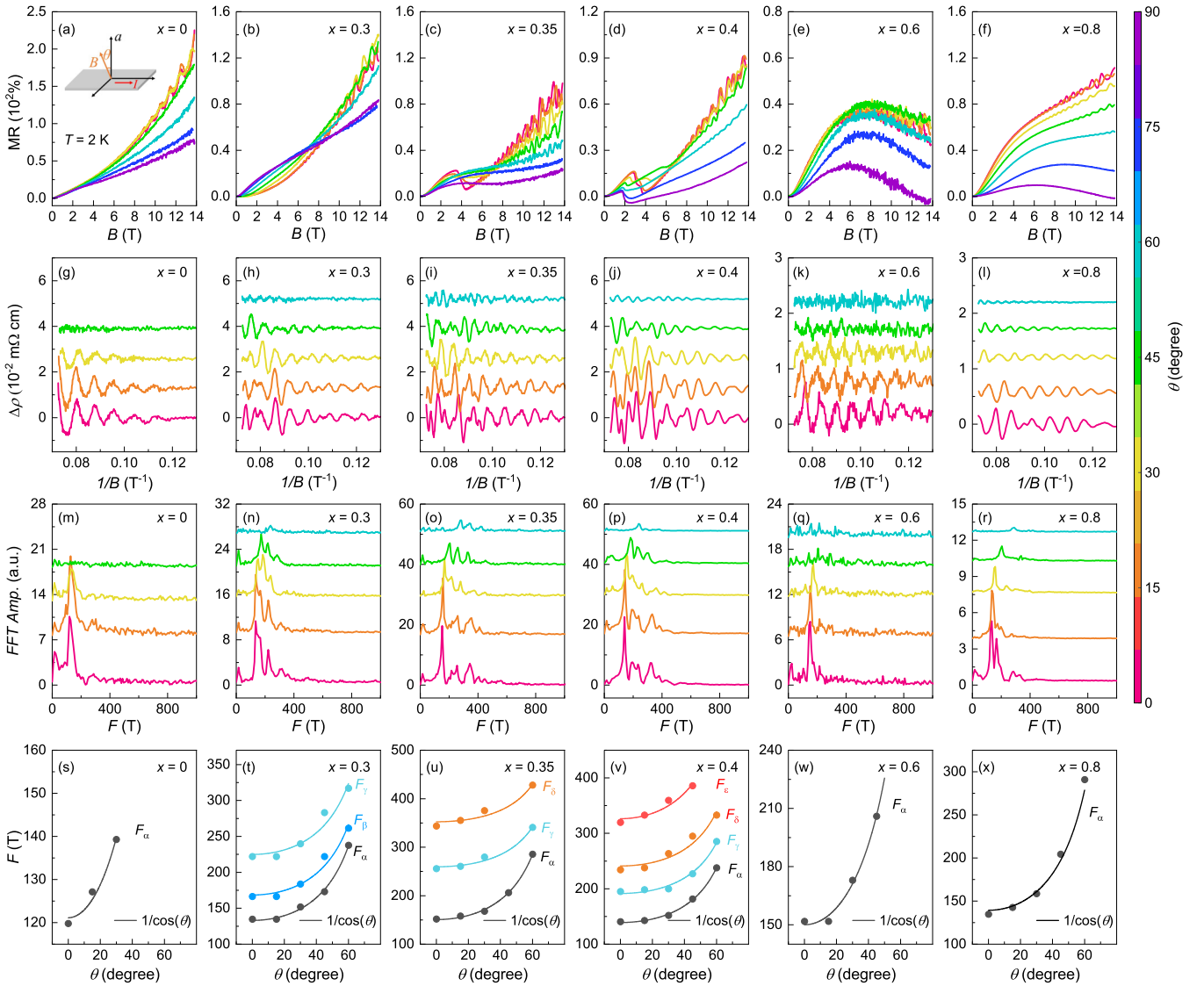


FIG. 4. (a)–(f) Quantum oscillation of  $\text{EuMn}_{1-x}\text{Zn}_x\text{Sb}_2$  ( $x = 0, 0.3, 0.35, 0.4, 0.6$ , and  $0.8$ ) at  $T = 2$  K under different magnetic field orientations ( $\theta = 0^\circ, 15^\circ, 30^\circ, 45^\circ, 60^\circ$ , and  $90^\circ$ ). The inset in (a) shows the configuration of the measurements. The oscillatory component of the resistivity at various magnetic field orientations (g)–(l) and corresponding FFT spectra (m)–(r). Data at different field orientations have been shifted for clarity. (s)–(x) The angular dependence of the oscillation frequencies obtained from the FFT spectra. The solid lines are fits to  $F = F_{3D} + F_{2D}/\cos(\theta)$ .

pockets around the  $\Gamma$  and  $Y$  point. The bands at  $Y$  point exhibit a linear band dispersion with a small gap, which is indicative of a massive Dirac semimetal [10,46]. The features of Fermi pockets around  $Y$  point match quite well with the main oscillation frequency  $F_\alpha$ , which has a good 2D/quasi-2D character with linear dispersion. Thus  $F_\alpha$  is therefore assigned to the tiny hole pocket at the  $Y$  point. Since  $F_\beta$  has a slightly higher frequency [Figs. 2(n) and 2(r)] and a similar angular dependence with  $F_\alpha$  [Fig. 4(t)],  $F_\beta$  might arise from the multiple extreme cross sections of the warped  $F_\alpha$  pocket, which is a common phenomenon in two-dimensional (2D) material with a cylindrical Fermi pocket. As Zn content  $x$  increases, the Fermi level is slightly decreased and touches the bands around the  $\Gamma$  point. Thus the doped samples' higher oscillation frequencies ( $F_\gamma$  and  $F_\delta$ ) can be assigned to the hole pockets around the  $\Gamma$  point. Notably, with increasing  $x$ , the conduction band formed by

the Zn  $4s$  orbital gradually decreases in energy and ultimately crosses the Fermi level, forming a new electron pocket at the  $\Gamma$  point in  $x = 0.625$  and  $1$ . Moreover, the carriers arising from Zn  $4s$  orbitals might have a lower mobility than that from the Sb  $5p$  orbital. Therefore, the electron pocket at  $\Gamma$  point may account for the carrier type change and absence of quantum oscillation in  $\text{EuZnSb}_2$  [Fig. 1(c)].

## F. Discussion

Our Zn doping study of  $\text{EuMn}_{1-x}\text{Zn}_x\text{Sb}_2$  aligns well with a complementary Sr doping study on  $\text{Eu}_{1-x}\text{Sr}_x\text{MnSb}_2$ , which finds that the transport properties depend sensitively on doping on the Eu site rather than that on the Mn site [21]. According to the orbital-resolved DOS and band structures (Figs. 5 and 6), both the Mn magnetism and Mn-derived

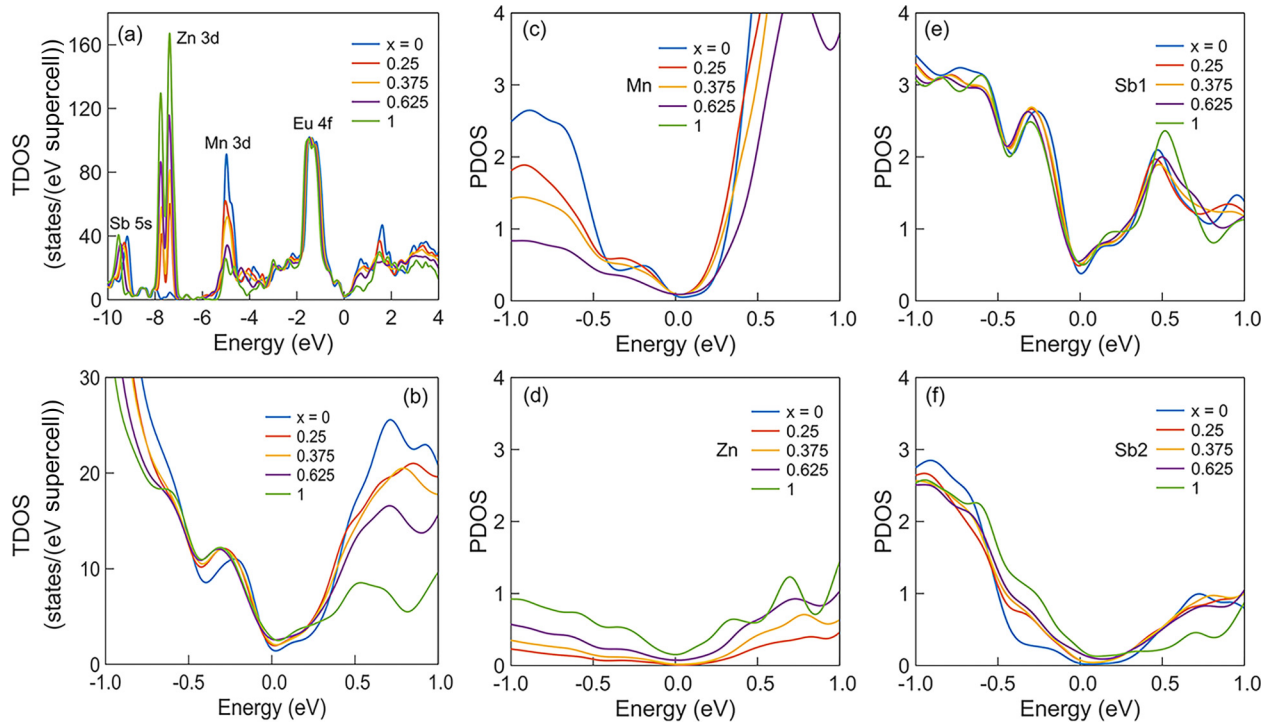


FIG. 5. Density of states (DOS) of the  $\text{EuMn}_{1-x}\text{Zn}_x\text{Sb}_2$  ( $x = 0, 0.25, 0.375,$  and  $0.625$ ). (a) The total density of states (TDOS) of the  $\text{EuMn}_{1-x}\text{Zn}_x\text{Sb}_2$  on a large energy scale, where the orbital character for each element can be identified. (b) The enlarged view of TDOS around the Fermi surface. (c)–(f) The atom-specific partial density of states (PDOS) for Mn, Zn, Sb1, and Sb2 components.

bands exert a limited influence on the physical properties of  $\text{EuMn}_{1-x}\text{Zn}_x\text{Sb}_2$ . Given that prior magnetic property studies have revealed a strong coupling between the Eu and Mn magnetic sublattice [15], it is likely that Mn indirectly

influences the Sb1-driven Dirac bands through its interaction with the Eu magnetic sublattice. The origin of the different coupling strengths between layers of Sb1-Eu and Sb1-Mn is rooted in the crystal structure character of  $\text{EuMn}_{1-x}\text{Zn}_x\text{Sb}_2$ .

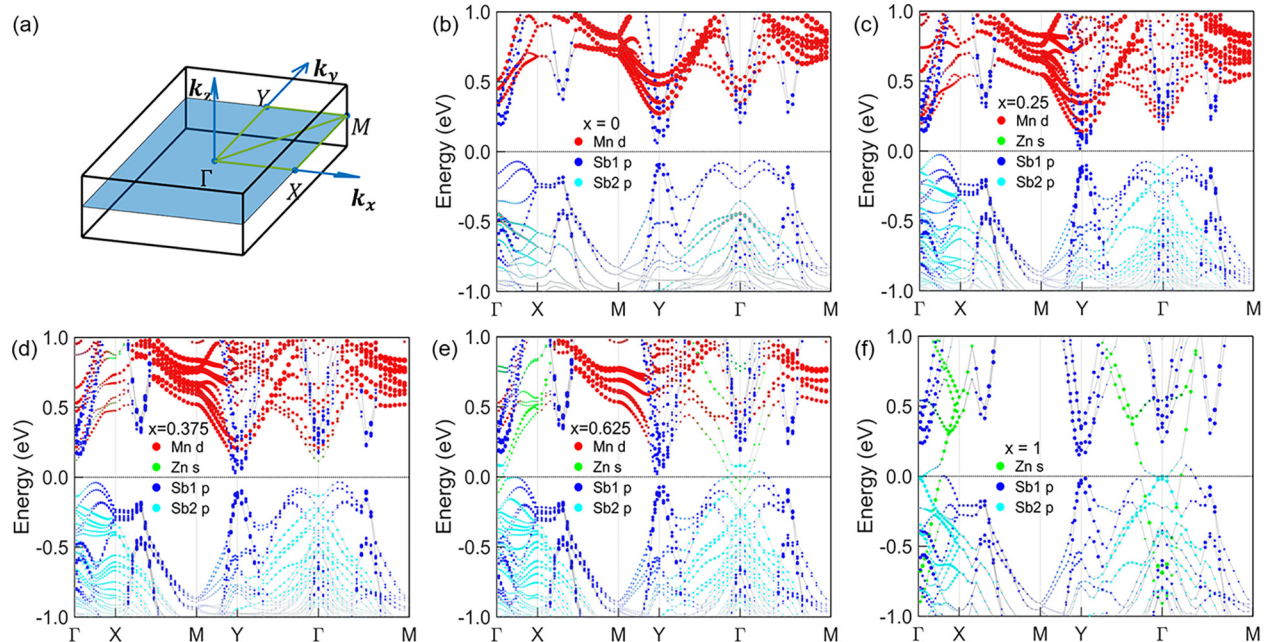


FIG. 6. (a) Brillouin zone of  $\text{EuMn}_{1-x}\text{Zn}_x\text{Sb}_2$  showing the highly symmetric paths used to calculate the energy bands. (b)–(f) The orbital projected band structure of  $\text{EuMn}_{1-x}\text{Zn}_x\text{Sb}_2$  ( $x = 0, 0.25, 0.375, 0.625,$  and  $1$ ), which were calculated using a  $1 \times 2 \times 1$  supercell with spin-orbit coupling (SOC). The area of the symbol is proportional to the contribution of the orbit.

As depicted in the crystal structure [Fig. 1(a)], the Sb1 layer containing the Dirac band is sandwiched by two types of AFM layer—specifically, an adjacent Eu layer and a more distant MnSb layer. According to this structure arrangement, it is reasonable that the Sb1 layer couples more strongly with Eu magnetism than with Mn.

#### IV. CONCLUSIONS

In conclusion, we have studied the evolution of electronic structures in  $\text{EuMn}_{1-x}\text{Zn}_x\text{Sb}_2$  ( $0 \leq x \leq 1$ ) via systematic magnetotransport measurements and DFT calculations. Clear quantum oscillation was observed for  $0 \leq x \leq 0.8$ . The analyses of quantum oscillation data reveal quasi-2D small Fermi pockets with light effective masses in the range of  $0 \leq x \leq 0.8$ . These findings suggest the electronic structure around the Fermi level is dominated by the Sb-driven Dirac bands, which are sensitive to the Eu magnetism and with a limited direct influence from Mn magnetism. Our study indicates that the Dirac dispersion, arising from Sb zigzag chains/square nets, has a stronger coupling with magnetism from neighboring elements than that from elements with a longer distance. This

could serve as a guideline for future exploration of a magnetic topological semimetal that exhibits strong coupling between the topological bands and magnetism.

#### ACKNOWLEDGMENTS

This work was financially supported in part by the National Natural Science Foundation of China (Grants No. 12004056, No. 11904040, No. 11974065, No. 52071041, No. 12104072, and No. 12147102), Chongqing Research Program of Basic Research and Frontier Technology, China (Grants No. cstc2021jcyj-msxmX0661, No. cstc2020jcyj-msxmX0263, and No. cstc2021jcyj-msxmX0640), the Fundamental Research Funds for the Central Universities of China (Grants No. 2022CDJXY-002 and No. 2023CDJXY-048), the Venture and Innovation Support Program for Chongqing Overseas Returnees (Grant No. cx2021050), and the Doctor “Through train” Scientific Research Project of Chongqing (Grant No. CSTB2022BSXM-JCX0087). We thank G. Wang at the Analytical and Testing Center of Chongqing University for her assistance with measurements. Numerical computations were performed at Hefei advanced computing center.

- 
- [1] L. Šmejkal, Y. Mokrousov, B. Yan, and A. H. MacDonald, *Nat. Phys.* **14**, 242 (2018).
- [2] Y. Tokura, K. Yasuda, and A. Tsukazaki, *Nat. Rev. Phys.* **1**, 126 (2019).
- [3] S. Klemenz, S. Lei, and L. M. Schoop, *Annu. Rev. Mater. Res.* **49**, 185 (2019).
- [4] S. Klemenz, L. Schoop, and J. Cano, *Phys. Rev. B* **101**, 165121 (2020).
- [5] G. Lee, M. A. Farhan, J. S. Kim, and J. H. Shim, *Phys. Rev. B* **87**, 245104 (2013).
- [6] H. Masuda, H. Sakai, M. Tokunaga, Y. Yamasaki, A. Miyake, J. Shiozaki, S. Nakamura, S. Awaji, A. Tsukazaki, H. Nakao, Y. Murakami, T.-H. Arima, Y. Tokura, and S. Ishiwata, *Sci. Adv.* **2**, e1501117 (2016).
- [7] J. Y. Liu, J. Yu, J. L. Ning, H. M. Yi, L. Miao, L. J. Min, Y. F. Zhao, W. Ning, K. A. Lopez, Y. L. Zhu, T. Pillsbury, Y. B. Zhang, Y. Wang, J. Hu, H. B. Cao, B. C. Chakoumakos, F. Balakirev, F. Weickert, M. Jaime, Y. Lai *et al.*, *Nat. Commun.* **12**, 4062 (2021).
- [8] J. Y. Liu, J. Hu, Q. Zhang, D. Graf, H. B. Cao, S. M. A. Radmanesh, D. J. Adams, Y. L. Zhu, G. Cheng, X. Liu, W. A. Phelan, J. Wei, M. Jaime, F. Balakirev, D. A. Tennant, J. F. DiTusa, I. Chiorescu, L. Spinu, and Z. Q. Mao, *Nat. Mater.* **16**, 905 (2017).
- [9] S. Borisenko, D. Evtushinsky, Q. Gibson, A. Yaresko, K. Koepnick, T. Kim, M. Ali, J. van den Brink, M. Hoesch, A. Fedorov, E. Haubold, Y. Kushnirenko, I. Soldatov, R. Schäfer, and R. J. Cava, *Nat. Commun.* **10**, 3424 (2019).
- [10] Z. L. Sun, A. F. Wang, H. M. Mu, H. H. Wang, Z. F. Wang, T. Wu, Z. Y. Wang, X. Y. Zhou, and X. H. Chen, *npj Quantum Mater.* **6**, 94 (2021).
- [11] J.-R. Soh, P. Manuel, N. M. B. Schröter, C. J. Yi, F. Orlandi, Y. G. Shi, D. Prabhakaran, and A. T. Boothroyd, *Phys. Rev. B* **100**, 174406 (2019).
- [12] D. Gong, S. Huang, F. Ye, X. Gui, J. Zhang, W. Xie, and R. Jin, *Phys. Rev. B* **101**, 224422 (2020).
- [13] J. M. Wilde, S. X. M. Riberolles, A. Das, Y. Liu, T. W. Heitmann, X. Wang, W. E. Straszheim, S. L. Bud'ko, P. C. Canfield, A. Kreyssig, R. J. McQueeney, D. H. Ryan, and B. G. Ueland, *Phys. Rev. B* **106**, 024420 (2022).
- [14] L. Zhang, Z. Sun, A. Wang, Y. Xia, X. Mi, L. Zhang, M. He, Y. Chai, T. Wu, R. Wang, X. Zhou, and X. Chen, *Phys. Rev. B* **104**, 205108 (2021).
- [15] Y. Xia, L. Wang, Y. Liu, L. Zhang, X. Wu, L. Zhang, T. Yang, K. Yang, M. He, Y. Chai, X. Zhou, and A. Wang, *Phys. Rev. B* **107**, 184415 (2023).
- [16] K. Zhao, X. Chen, Z. Wang, J. Liu, J. Wu, C. Xi, X. Lv, L. Li, Z. Zhong, and P. Gegenwart, *Phys. Rev. B* **107**, L081112 (2023).
- [17] G. Kresse and J. Furthmüller, *Phys. Rev. B* **54**, 11169 (1996).
- [18] P. E. Blöchl, *Phys. Rev. B* **50**, 17953 (1994).
- [19] See Supplemental Material at <http://link.aps.org/supplemental/10.1103/PhysRevB.108.165115> for Hall angle, MR behavior, spin flop transition, doping dependence of oscillation frequency and effective mass, and more details about the electronic structure.
- [20] J. P. Perdew, J. A. Chevary, S. H. Vosko, K. A. Jackson, M. R. Pederson, D. J. Singh, and C. Fiolhais, *Phys. Rev. B* **46**, 6671 (1992).
- [21] Q. Zhang, J. Liu, H. Cao, A. Phelan, D. Graf, J. F. DiTusa, D. A. Tennant, and Z. Mao, *NPG Asia Mater.* **14**, 22 (2022).
- [22] C. Yi, S. Yang, M. Yang, L. Wang, Y. Matsushita, S. Miao, Y. Jiao, J. Cheng, Y. Li, K. Yamaura, Y. Shi, and J. Luo, *Phys. Rev. B* **96**, 205103 (2017).
- [23] Y.-Y. Wang, S. Xu, L.-L. Sun, and T.-L. Xia, *Phys. Rev. Mater.* **2**, 021201(R) (2018).
- [24] A. Pippard, *Magnetoresistance in Metals*, Cambridge Studies in Low Temperature Physics (Cambridge University Press, Cambridge, UK, 1989).

- [25] A. Wang, D. Graf, Y. Liu, Q. Du, J. Zheng, H. Lei, and C. Petrovic, *Phys. Rev. B* **96**, 121107(R) (2017).
- [26] J. Hu and T. F. Rosenbaum, *Nat. Mater.* **7**, 697 (2008).
- [27] K. Wang, D. Graf, H. Lei, S. W. Tozer, and C. Petrovic, *Phys. Rev. B* **84**, 220401(R) (2011).
- [28] D. Shoenberg, *Magnetic Oscillations in Metals*, Cambridge Monographs on Physics (Cambridge University Press, Cambridge, UK, 1984).
- [29] N. Ashcroft and N. Mermin, *Solid State Physics* (Cengage, Boston, 1976).
- [30] J. Park, G. Lee, F. Wolff-Fabris, Y. Y. Koh, M. J. Eom, Y. K. Kim, M. A. Farhan, Y. J. Jo, C. Kim, J. H. Shim, and J. S. Kim, *Phys. Rev. Lett.* **107**, 126402 (2011).
- [31] J. Liu, P. Liu, K. Gordon, E. Emmanouilidou, J. Xing, D. Graf, B. C. Chakoumakos, Y. Wu, H. Cao, D. Dessau, Q. Liu, and N. Ni, *Phys. Rev. B* **100**, 195123 (2019).
- [32] J. B. He, Y. Fu, L. X. Zhao, H. Liang, D. Chen, Y. M. Leng, X. M. Wang, J. Li, S. Zhang, M. Q. Xue, C. H. Li, P. Zhang, Z. A. Ren, and G. F. Chen, *Phys. Rev. B* **95**, 045128 (2017).
- [33] S. Huang, J. Kim, W. A. Shelton, E. W. Plummer, and R. Jin, *Proc. Natl. Acad. Sci. USA* **114**, 6256 (2017).
- [34] K. Wang, D. Graf, L. Wang, H. Lei, S. W. Tozer, and C. Petrovic, *Phys. Rev. B* **85**, 041101(R) (2012).
- [35] A. Wang, I. Zaliznyak, W. Ren, L. Wu, D. Graf, V. O. Garlea, J. B. Warren, E. Bozin, Y. Zhu, and C. Petrovic, *Phys. Rev. B* **94**, 165161 (2016).
- [36] C. M. Wang, H.-Z. Lu, and S.-Q. Shen, *Phys. Rev. Lett.* **117**, 077201 (2016).
- [37] Q. Jiang, C. Wang, P. Malinowski, Z. Liu, Y. Shi, Z. Lin, Z. Fei, T. Song, D. Graf, S. Chikara, X. Xu, J. Yan, D. Xiao, and J.-H. Chu, *Phys. Rev. B* **103**, 205111 (2021).
- [38] M. Lyu, J. Xiang, Z. Mi, H. Zhao, Z. Wang, E. Liu, G. Chen, Z. Ren, G. Li, and P. Sun, *Phys. Rev. B* **102**, 085143 (2020).
- [39] N. Zhang, X. Ding, F. Zhan, H. Li, H. Li, K. Tang, Y. Qian, S. Pan, X. Xiao, J. Zhang, R. Wang, Z. Xiang, and X. Chen, *Phys. Rev. Res.* **5**, L022013 (2023).
- [40] J. Wosnitza, G. Goll, A. D. Bianchi, B. Bergk, N. Kozlova, I. Opahle, S. Elgazzar, M. Richter, O. Stockert, H. v. Löhneysen, T. Yoshino, and T. Takabatake, *New J. Phys.* **8**, 174 (2006).
- [41] J. Hu, Z. Tang, J. Liu, Y. Zhu, J. Wei, and Z. Mao, *Phys. Rev. B* **96**, 045127 (2017).
- [42] T. Berlijn, C.-H. Lin, W. Garber, and W. Ku, *Phys. Rev. Lett.* **108**, 207003 (2012).
- [43] S. Ideta, T. Yoshida, M. Nakajima, W. Malaeb, T. Shimojima, K. Ishizaka, A. Fujimori, H. Kimigashira, K. Ono, K. Kihou, Y. Tomioka, C. H. Lee, A. Iyo, H. Eisaki, T. Ito, and S. Uchida, *Phys. Rev. B* **87**, 201110(R) (2013).
- [44] J. An, A. S. Sefat, D. J. Singh, and M.-H. Du, *Phys. Rev. B* **79**, 075120 (2009).
- [45] A. Wang, S. Baranets, Y. Liu, X. Tong, E. Stavitski, J. Zhang, Y. Chai, W.-G. Yin, S. Bobev, and C. Petrovic, *Phys. Rev. Res.* **2**, 033462 (2020).
- [46] H. Rong, L. Zhou, J. He, C. Song, J. Huang, C. Hu, Y. Xu, Y. Cai, H. Chen, C. Li, Q. Wang, L. Zhao, Z. Zhu, G. Liu, Z. Xu, G. Chen, H. Weng, and X. J. Zhou, *Phys. Rev. B* **103**, 245104 (2021).